Supporting Information

Advanced Oxygen-Electrode-Supported Solid Oxide Electrochemical Cells with $Sr(Ti,Fe)O_{3-\delta}$-based Fuel Electrodes for Electricity Generation and Hydrogen Production

Shan-Lin Zhang,[ab] Hongqian Wang,[a] Tianrang Yang,[a] Matthew Y. Lu,[a] Cheng-Xin Li,[b*]

Chang-Jiu Li,[b*] and Scott A. Barnett [a*]

[a] Department of Materials Science and Engineering, Northwestern University, Evanston, Illinois 60208, USA

b State Key laboratory for Mechanical Behavior of Materials, School of Materials Science and Engineering, Xi'an Jiaotong University, Xi'an, Shaanxi, 710049, People's Republic of China

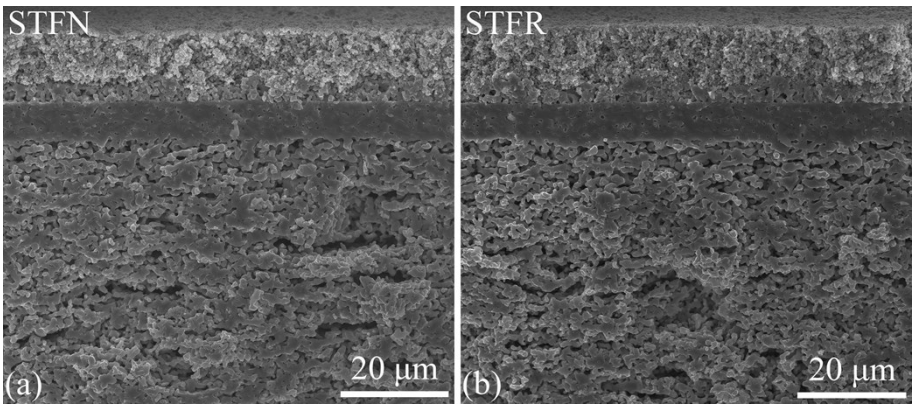

Fig. S1. Fracture cross sectional SEM images giving an overview of the cells with STFN (a) and STFR (b) electrodes.

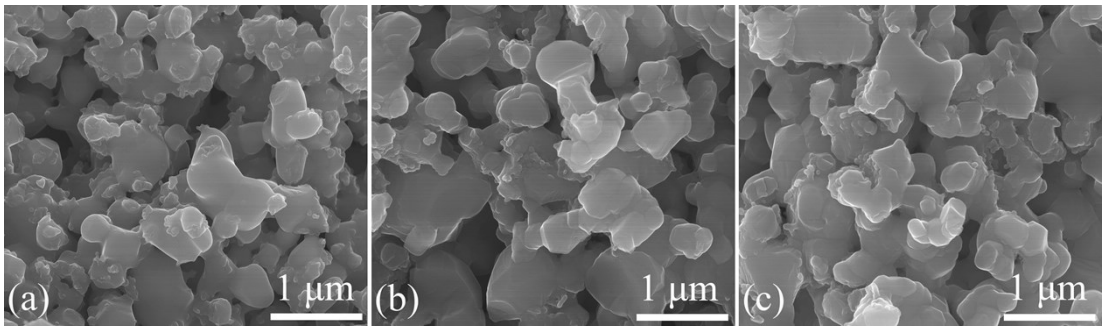

Fig. S2. Fracture cross sectional SEM images showing the microstructures of as-prepared STF (a), STFN (b), and STFR (c) electrodes.

Fig. S3 shows polished cross-sectional images of the STF-based electrodes after the cell test. The structures are porous with well-connected electrode particles and there is no significant difference between the different electrodes because they were prepared using the similar materials and the same procedures. The exsolved nano particles in the STFN and STFR electrodes are not large enough to be resolved at this magnification. Fig. S4 shows the porosity (a), specific surface area (b), and solid phase tortuosity factor (c) of the STF-based electrodes obtained from stereological analysis of the images in Fig. S3. The STF-based electrodes were found to have a similar porosity of 38–40% with a similar specific surface area a of 4.55–4.68 μm^{-1} and a similar solid phase tortuosity factor of 1.24–1.26. The present STFN and STFR electrodes are found to have approximately the same microstructure as the STF, aside from the nanoparticles.

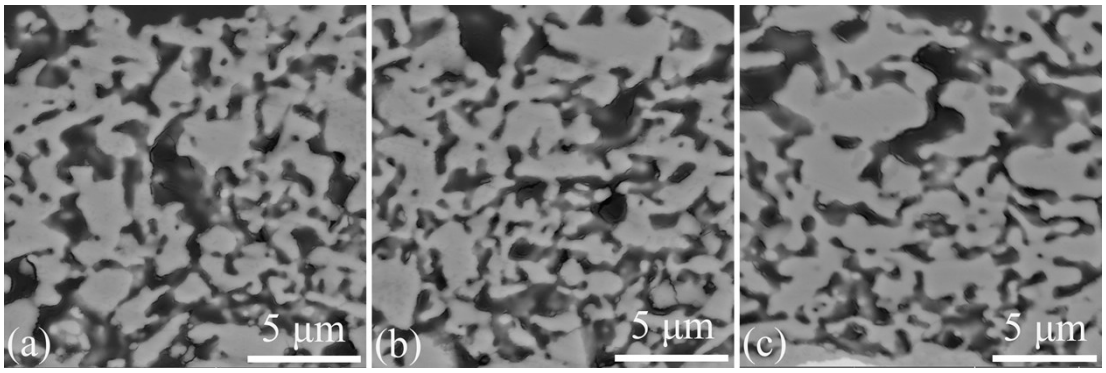

Fig. S3. Polished cross-sectional images of STF (a), STFN (b), and STFR (c) electrodes.

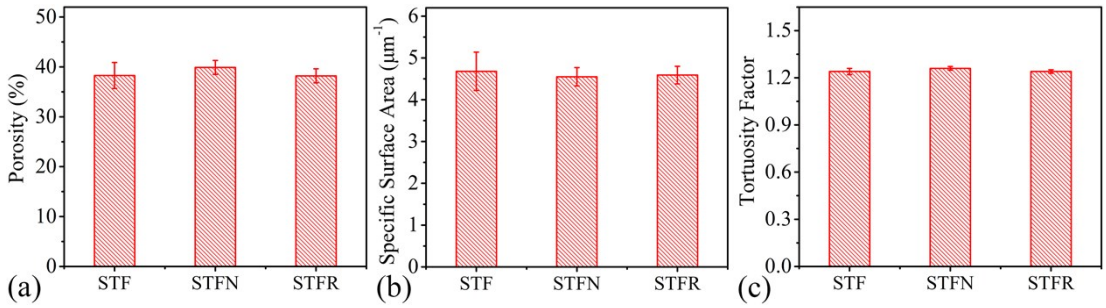

Fig. S4. Electrode porosity (a), specific surface area (b), and solid phase tortuosity factor (c) derived from stereological analysis of the STF, STFN, and STFR electrode images shown in Fig. S3.

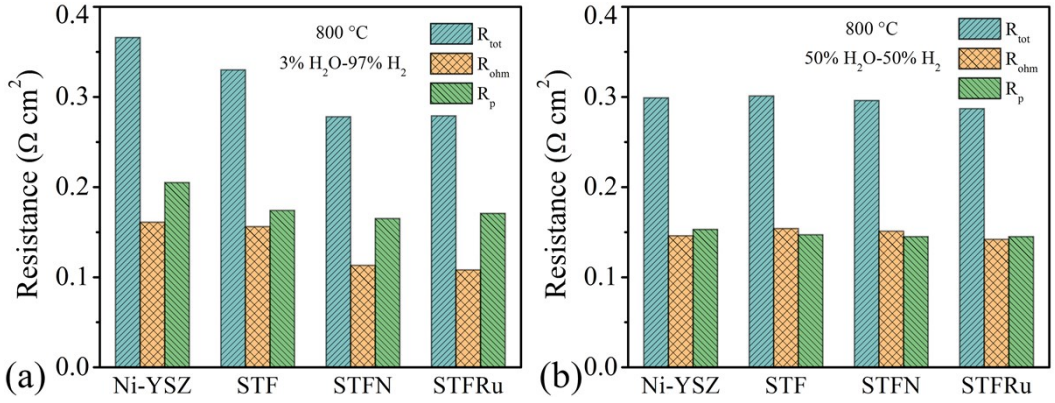

Fig. S5. Resistance values from the EIS date for the full cells with different fuel electrodes tested at 800 °C, (a) 3% H_2O-97% H_2, (b) 50% H_2O-50% H_2.

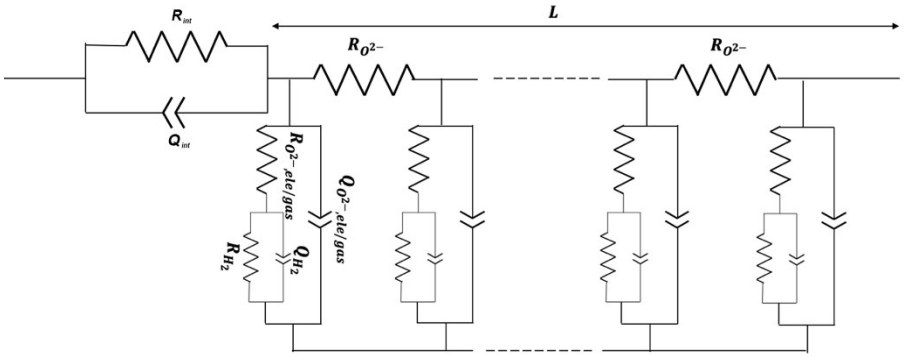

Fig. S6. Schematic of the equivalent circuit. $R_{O^{2-}}$: ionic conductivity of the electrode; $R_{elec/gas}Q_{elec/gas}$: the hydrogen oxidation reaction at the electrode/gas interface; $R_{int}Q_{int}$: representing an interfacial process; $R_{H_2}Q_{H_2}$: representing hydrogen adsorption

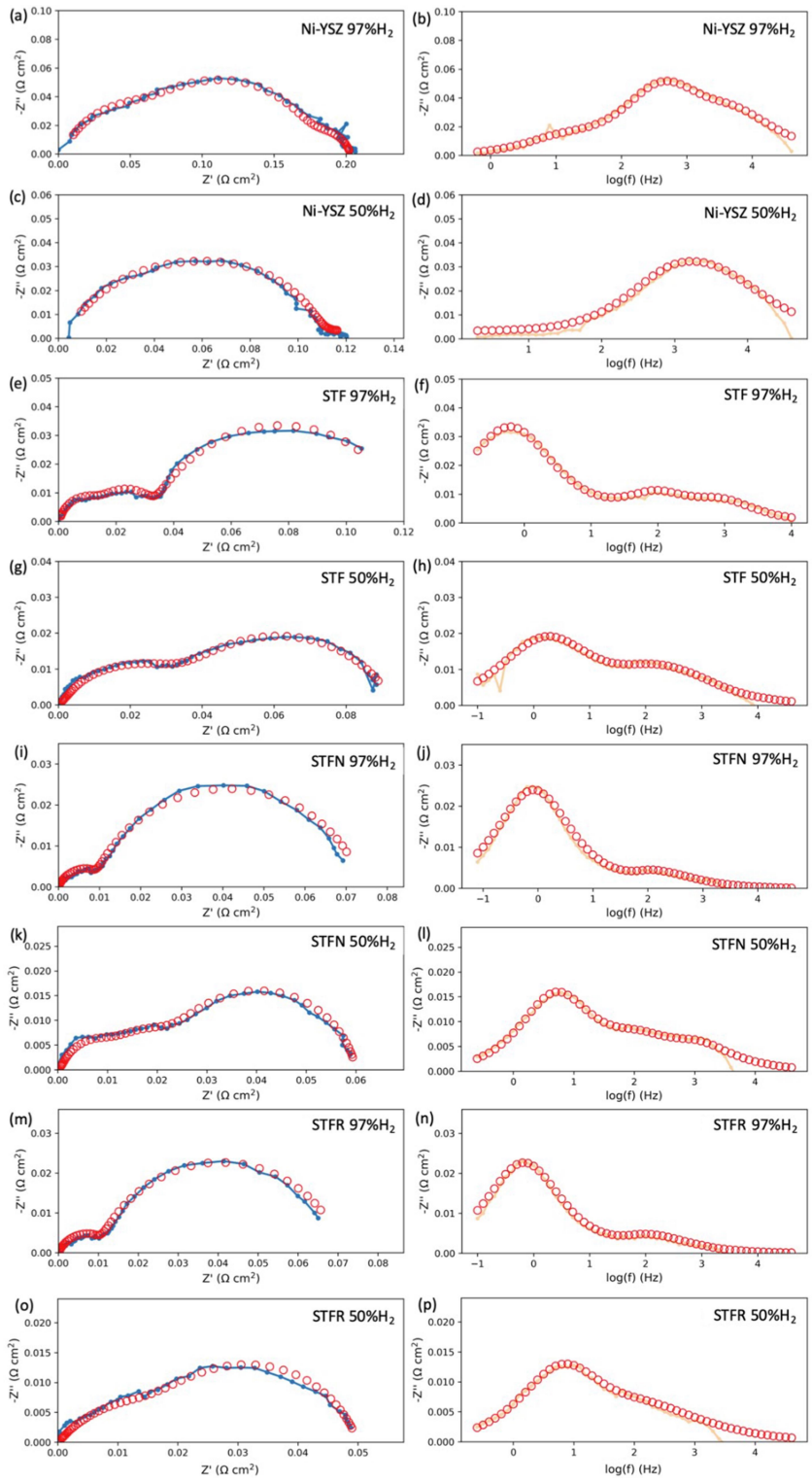

Fig. S7. Nyquist and Bode plots of symmetrical cells at 97%H_2+3%H_2O and 50%H_2-50%H_2O with (a) (b) (c) (d) Ni-YSZ, (e) (f) (g) (h) STF, (i) (j) (k) (l) STFN, and (m) (n) (o) (p) STFR as electrodes. The solid lines and red open circles are experimental and fitting data, respectively. Blue dots and lines are experimental data. Red circles are fitted results.

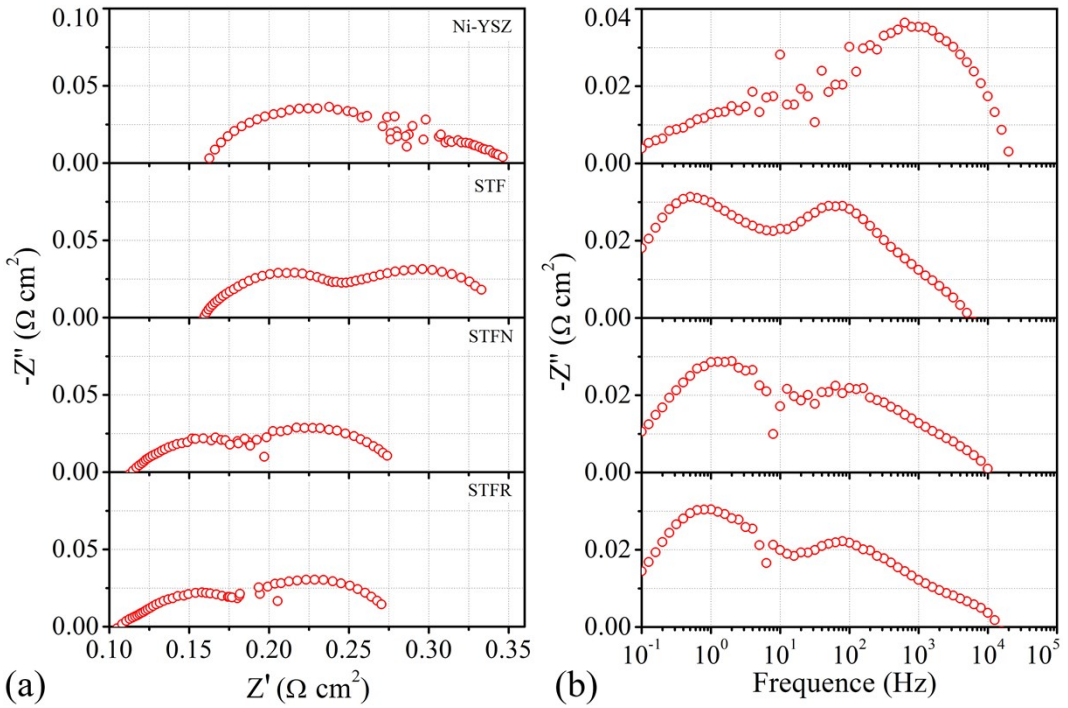

Fig. S8. Nyquist (a) and Bode plots (b) of EIS data for OESCs with different fuel electrodes measured at 3% H_2O + 97% H_2 and 800 °C. Air was supplied to the oxygen electrode sides.

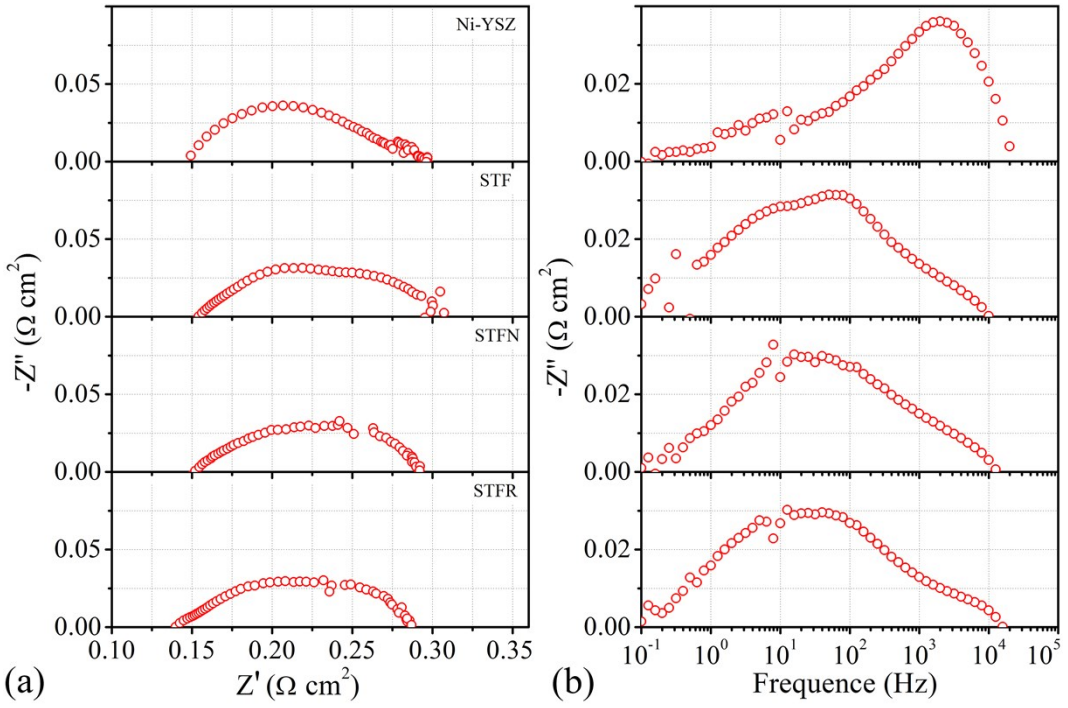

Fig. S9. Nyquist (a) and Bode plots (b) of EIS data for OESCs with different fuel electrodes

measured at 50% H_2O + 50% H_2 and 800 °C. Air was supplied to the oxygen electrode sides.

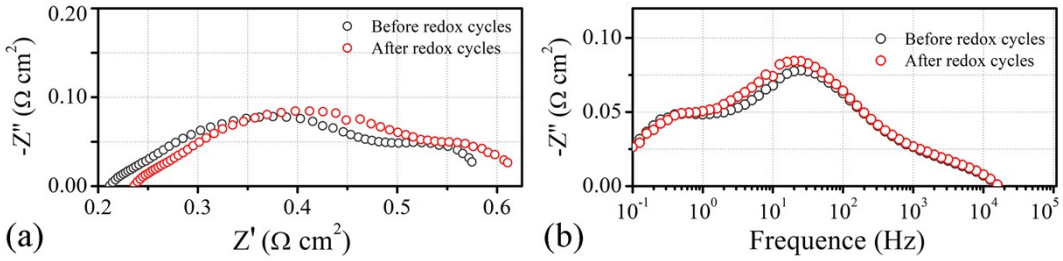

Fig. S10. Nyquist (a) and Bode (b) plots of EIS data for the STF cell before and after redox cycles.

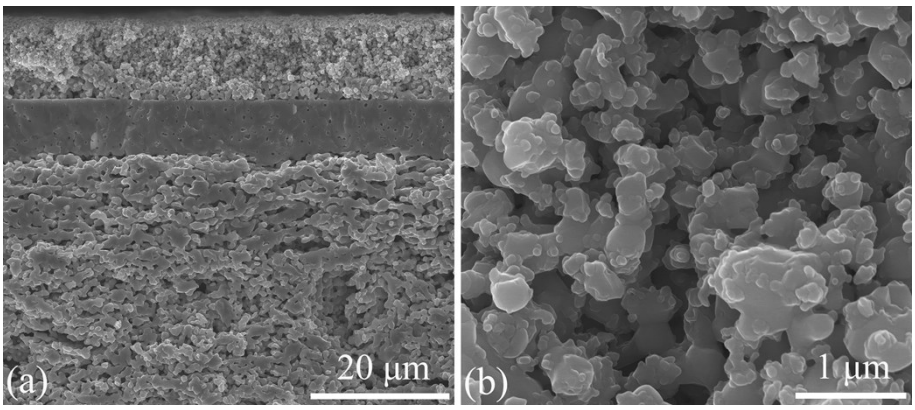

Fig. S11. Fractured cross-sectional images of the full cell (a) and STF fuel electrode (b) taken after 10 redox cycling testing.

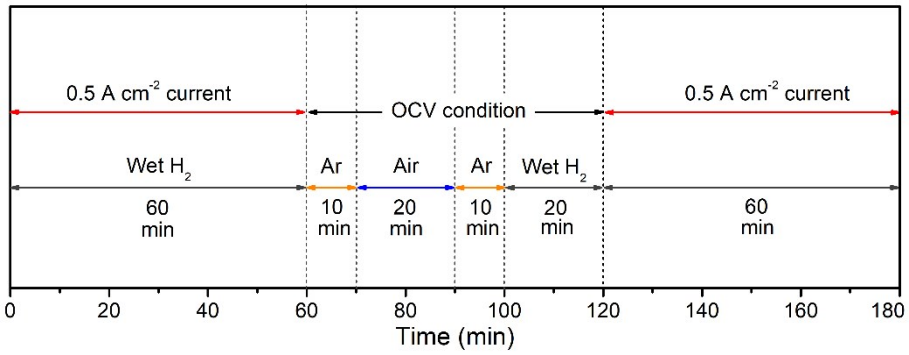

Fig. S12. The configuration of experimental conditions of the redox testing.